Inorg. Chem. **XXXX**, *xx*, 0

Structural and Physical Characterization of Tetranuclear [$Mn^{II}_3Mn^{IV}$] and [$Mn^{II}_2Mn^{III}_2$] Valence-Isomer Manganese Complexes

Curtis M. Zaleski,[§] Tsu-Chen Weng,[‡] Catherine Dendrinou-Samara,[†] Maria Alexiou,[†] Paraskevi Kanakaraki,[†] Wen-Yuan Hsieh,[‡] Jeff Kampf,[‡] James E. Penner-Hahn,*[,‡] Vincent L. Pecoraro,*[,‡] and Dimitris P. Kessissoglou*[,†]

Department of Chemistry, Aristotle University of Thessaloniki, Thessaloniki, 54124, Greece, Department of Chemistry, University of Michigan, Ann Arbor, Michigan 48109-1055, and Department of Chemistry, Shippensburg University, Pennsylvania 17257-2200

Received October 25, 2007

Two tetranuclear Mn complexes with an average Mn oxidation state of +2.5 have been prepared. These valence isomers have been characterized by a combination of X-ray crystallography, X-ray absorption spectroscopy, and magnetic susceptibility. The $Mn^{II}_3Mn^{IV}$ tetramer has the Mn ions arranged in a distorted tetrahedron, with an $S = 6$ ground spin state, dominated by ferromagnetic exchange among the manganese ions. The $Mn^{II}_2Mn^{III}_2$ tetramer also has a distorted tetrahedral arrangement of Mn ions but shows magnetic behavior, suggesting that it is a single-molecule magnet. The X-ray absorption near-edge structure (XANES) spectra for the two complexes are similar, suggesting that, while Mn XANES has sufficient sensitivity to distinguish between trinuclear valence isomers (Alexiou et al. *Inorg. Chem.* **2003**, *42*, 2185), similar distinctions are difficult for tetranuclear complexes such as that found in the photosynthetic oxygen-evolving complex.

Introduction

One of the most important biochemical processes is the photosynthetic conversion of water to dioxygen, which occurs in the oxygen evolving complex (OEC) of photosystem II (PSII). One calcium and four manganese ions form the heart of the water oxidation machinery of this enzyme.[1,2] There are five resolvable enzyme oxidation levels, termed S states, with the most reduced form being the S_0 level and the liberation of dioxygen occurring on the $S_3 \rightarrow S_4 \rightarrow S_0$ transition.[3] Chloride serves as an essential anion; however, whether the chloride is directly bound to manganese or calcium is under debate.[4] In recent years, one of the most contentious areas associated with water oxidation chemistry has been the assignment of oxidation states to the manganese ions in each enzyme oxidation level. Probably the most controversial issue has been whether the manganese ions or substrate are oxidized from an $Mn^{III}Mn_3^{IV}$ in S_2 to either Mn_4^{IV} or $Mn^{III}Mn_3^{IV}$/radical species in S_3.[4] Another unresolved issue is the oxidation level of the manganese ions in the S state produced after water oxidation. The manganese oxidation levels in the S_0 state have alternatively been assigned as $Mn^{II}Mn^{III}Mn_2^{IV}$ or $Mn_3^{III}Mn^{IV}$.[4] Clearly, a full understanding of the water oxidation mechanism requires a definitive answer for the proper metal oxidation states in each enzyme form.

Numerous techniques have been used to probe the oxidation states of the manganese ions in the different S states, with X-ray absorption spectroscopy (XAS)[4] and electron paramagnetic resonance (EPR) spectroscopy[5,6] being the most valuable. Critical to this assignment has been the interpretation of the X-ray absorption near-edge structure

* Authors to whom correspondence should be addressed. E-mail: jeph@umich.edu (J.E.P.-H.), vlpec@umich.edu (V.L.P.), kessisog@chem.auth.gr (D.P.K.).
† Aristotle University of Thessaloniki.
‡ University of Michigan.
§ Shippensburg University.

(1) (a) Pecoraro, V. L.; Hsieh, W.-Y. In *Manganese and Its Role in Biological Processes*; Sigel, A., Sigel, H., Eds.; Marcel Dekker: New York, 2000; Vol. *37*, pp 429. (b) Wydrzynski, T. J.; Satoh, K. *Photosystem II: The Light-Driven Water: Plastoquinone Oxidoreductase*; Springer: Dordrecht, The Netherlands, 2005. (c) Tommos, C.; Babcock, G. T. *Acc. Chem. Res.* **1998**, *31*, 18. (d) McEvoy, J. P.; Brudvig, G. W. *Chem. Rev.* **2006**, *106*, 4455. (e) Yocum, C. F.; Pecoraro, V. L. *Curr. Opin. Chem. Biol.* **1999**, *3*, 182. (f) Yachandra, V. K.; Sauer, K.; Klein, M. P. *Chem. Rev.* **1996**, *96*, 2927.
(2) Carrell, T. G.; Tyryshkin, A. M.; Dismukes, G. C. *J. Biol. Inorg. Chem.* **2002**, *7*, 2.
(3) Kok, B.; Forbush, B.; McGloid, M. *Photochem. Photobiol.* **1970**, *11*, 457.
(4) Mukhopadhyay, S.; Mundal, S. K.; Bhaduri, S.; Armstrong, W. H. *Chem. Rev.* **2004**, *104*, 3981.

10.1021/ic702109c CCC: $40.75
Published on Web 06/07/2008

(XANES) of the S_0 state. In order to correctly interpret XANES data, a catalogue of relevant model compounds is required. Previously, we showed that the proper assignment of the manganese oxidation state could be achieved using XANES spectroscopy for valence isomers of Mn_3^{8+} compounds [$Mn_2^{II}Mn^{IV}$ (**3**) vs $Mn^{II}Mn_2^{III}$ (**4**)].[8] In the present work, we extend this study to a novel pair of tetranuclear valence isomers of Mn_4^{+10} with overall oxidation states of 2.5+/Mn.

Several tetranuclear mixed valence manganese complexes have been prepared as potential models for the OEC of PSII.[9–23] Christou and co-workers[10,11] and Brudvig and coworkers[15,16] have shown that, under appropriate conditions, monofunctional carboxylato ligands support the formation of the so-called butterfly-type tetranuclear complexes. However, these and other carboxylato systems are relatively labile and tend to aggregate further. To date, the lowest-valence tetranuclear complexes, with an average oxidation state of 2.5+/Mn ($Mn_2^{II}Mn_2^{III}$ or $Mn_3^{II}Mn^{IV}$ formulations), have been reported with formulas of $[Mn_4O(AcO)_2(H_2O)_2(tphpn)_2]^{4+}$ {tphpn = $[(o\text{-}py)CH_2]_2NCH_2CH(O^-)CH_2N[CH_2(o\text{-}py)]_2$}, having a linear ($\mu$-O)$Mn_2$ bridging moiety, $[Mn_4O_2(Ph_3COO)_6)_2(OEt_2)_2]$, with a ($\mu_3$-O)Mn bridging moiety,[23,24] and $Mn_4(O)(pko)_4(3,4\text{-}D)_4$ {(Hpko = dipyridylketoxime; H-3,4-D = 3,4-dichlorophenoxy-acetic acid}, with a (μ_4-O)Mn bridging moiety.[25] The average oxidation state 2.75+/Mn is represented by two formulations: $Mn^{II}Mn^{III}_3$ in the compound $[Mn_4O_2(X\text{-}PhCOO)_7(bpy)_2]$ (X = Cl, Br)[26] with (μ_3-O)Mn_3 bridging group and $Mn^{II}_2Mn^{III}Mn^{IV}$ in the compound $[Mn_4O_2(H_2O)_2(CF_3SO_3)_2(tphpn)_2]^{3+}$ with a (μ-O)Mn_2 bridging moiety.[27] The average oxidation state 3.0+/Mn is found only for the Mn^{III}_4 formulation. Characteristic examples are $[Mn_4O_2(MeCOO)_6(py)_2(dbm)_2]$[28] (dbm = dibenzoylmethane) and $(Nbu_4)[Mn_4O_2(X\text{-}PhCOO)_9(H_2O)]$[29] with ($\mu$-O)$Mn_2$ bridging groups. The average oxidation states 3.25+/Mn and 3.50+/Mn are considered the most likely to represent the S_0 and the S_1 states of the OEC, respectively. Formulations reported to date are $Mn^{III}_3Mn^{IV}$ and $Mn^{III}_2Mn^{IV}_2$. The compounds $(H_2Im)_2[Mn_4O_3Cl_6(MeCOO)_6(HIm)]$, $[Mn_4O_3Cl_4(MeCOO)_3(py)_3]$, and $[Mn_4O_3Cl(MeCOO)_3(dbm)_3]$ (HIm = imidazolium) have a distorted cubane $[Mn_4O_3Cl]$ core with (μ_3-O)Mn_3 bridging groups[28,30,31] and an average oxidation state of +3.25/Mn, while $[(Mn_2O_2)_2(tphpn)_2]^{4+}$, with ($\mu$-O)$Mn_2$ bridging atoms,[22,32] is an example of +3.5/Mn. Average oxidation states of 3.75+/Mn with a $Mn^{III}Mn^{IV}_3$ formulation and 4.00/Mn with a Mn^{IV}_4 formulation have also been reported.[33] The former is the most likely oxidation state for the S_2 state of the OEC.

In this report, we describe the synthesis and characterization of two Mn_4^{10+} tetramers that may serve as models for the lower S states of the OEC, and we explore the ability of XANES spectroscopy to accurately assign oxidation states for $Mn^{II}_3Mn^{IV}$ versus $Mn^{II}_2Mn^{III}_2$ in order to test in principle whether the oxidation level of the Mn ions in the OEC can be assigned reliably. In doing so, we provide an example of a 1-D-chain manganese polymer consisting of tetranuclear complexes having the $[Mn^{II}_2Mn^{III}_2]^{10+}$ core and a second example of a tetranuclear complex having the $[Mn^{II}_3Mn^{IV}]^{10+}$ core. Compound **2**, with the formulation $Mn^{II}_2Mn^{III}_2(pko)_2(pdiol)_2(N_3)_6(CH_3OH)_2$ (H_2pdiol = dipyridylketodiol), is also the only example with three different coordination modes of the azido ligand in the same molecule. Finally, we examine the magnetic behavior of these complexes and compare them to the class of molecules known as single-molecule magnets (SMMs).

Experimental Section

Materials. The chemicals for the synthesis of the compounds were used as purchased. *N*,*N*-dimethylformamide (DMF) was distilled from CaH_2 and CH_3OH from Mg, and these were stored

(5) Yachandra, V. K.; Guiles, R. D. ; McDermott, A.; Britt, R. D.; Cole, J.; Dexheimer, S. L.; Sauer, K.; Klein, M. P. *J. Phys., Colloq.* **1986**, *C8*, 2.
(6) Åhrling, K. A.; Peterson, S.; Styring, S. *Biochemistry* **1997**, *36*, 13148.
(7) Messinger, J.; Robblee, J. H.; Yu, W. O.; Sauer, K.; Yachandra, V. K.; Klein, M. P. *J. Am. Chem. Soc.* **1997**, *119*, 11349.
(8) Alexiou, M.; Dendrinou-Samara, C.; Karagianni, A.; Biswas, S.; Zaleski, C. M.; Kampf, J. W.; Yoder, D.; Penner-Hahn, J. E.; Pecoraro, V. L.; Kessissoglou, D. P. *Inorg. Chem.* **2003**, *42*, 2185.
(9) Christou, G. *Acc. Chem. Res.* **1989**, *22*, 328.
(10) Schake, A. R.; Schmitt, E. A.; Conti, A. J.; Streib, W. E.; Huffman, J. C.; Hendrickson, D. N.; Christou, G. *Inorg. Chem.* **1991**, *30*, 3192.
(11) Folting, K.; Huffman, J. C.; Christou, G.; Hendrickson, D. N. *J. Am. Chem. Soc.* **1987**, *109*, 5703.
(12) Guiles, R. D.; McDermott, A.; Yachandra, V. K.; Cole, J. L.; Dexheimer, S. L.; Britt, R. D.; Wieghardt, K.; Bossek, U.; Sauer, K.; Klein, M. P. *Biochemistry* **1990**, *29*, 471.
(13) Wieghardt, K. *Angew. Chem., Int. Ed. Engl.* **1989**, *28*, 1153.
(14) Hotzelmann, R.; Wieghardt, K.; Florke, U.; Haupt, H.-J.; Weatherburn, D. C.; Bonvoisin, J.; Blondin, G.; Girerd, J.-J. *J. Am. Chem. Soc.* **1992**, *114*, 1681.
(15) Manchanda, R.; Thorp, H. H.; Brudvig, G. W.; Crabtree, R. H. *Inorg. Chem.* **1991**, *30*, 494.
(16) Brudvig, G. W.; Crabtree, R. H. *Prog. Inorg. Chem.* **1989**, *37*, 99.
(17) Vincent, J. B.; Christou, G. *Adv. Inorg. Chem.* **1989**, *33*, 197.
(18) Low, D.; Eichorn, D. M.; Draganescu, A.; Armstrong, W. H. *Inorg. Chem.* **1991**, *30*, 877.
(19) Hagen, K. S.; Armstrong, W. H.; Olmstead, M. M. *J. Am. Chem. Soc.* **1989**, *111*, 774.
(20) Chan, M. K.; Armstrong, W. H. *J. Am. Chem. Soc.* **1991**, *113*, 5055.
(21) Chan, M. K.; Armstrong, W. H. *J. Am. Chem. Soc.* **1989**, *111*, 9121.
(22) Chan, M. K.; Armstrong, W. H. *J. Am. Chem. Soc.* **1990**, *112*, 4985.
(23) Kulawiec, R. J.; Crabtree, R. H.; Brudvig, G. W.; Schulte, G. K. *Inorg. Chem.* **1988**, *27*, 1309.
(24) Wang, S.; Huffman, J. C.; Streib, W. E.; Schmitt, E. A.; McCusker, J. K.; Hendrickson, D. N.; Christou, G. *Angew. Chem., Int. Ed. Engl.* **1991**, *30*, 305.
(25) Afrati, T.; Dendrinou-Samara, C.; Raptopoulou, C. P.; Terzis, A.; Tangoulis, V.; Kessissoglou, D. P. *Angew. Chem., Int. Ed.* **2002**, *41*, 2148.
(26) Wang, S.; Huffman, J. C.; Folting, K.; Streib, W. E.; Lobkovsky, E. B.; Christou, G. *Angew. Chem., Int. Ed. Engl.* **1991**, *30*, 1672.
(27) Albela, B.; Salah, M. S. E.; Ribas, J.; Folting, K.; Christou, G.; Hendrickson, D. N. *Inorg. Chem.* **2001**, *40*, 1037.
(28) Bashkin, J. S.; Chang, H.-R.; Streib, W. E.; Huffman, J. C.; Hendrickson, D. N.; Christou, G. *J. Am. Chem. Soc.* **1987**, *109*, 6502.
(29) Hendrickson, D. N.; Christou, G.; Schmitt, E. A.; Libby, E.; Bashkin, J. S.; Wang, S.; Tsai, H.-L.; Vincent, J. B.; Boyd, P. D. W.; Huffman, J. C.; Folting, K.; Li, Q.; Streib, W. E. *J. Am. Chem. Soc.* **1992**, *114*, 2455.
(30) Randall, D. W.; Sturgeon, B. E.; Ball, J. A.; Lorigan, G. A.; Chan, M. K.; Klein, M. P.; Armstrong, W. H.; Britt, R. D. *J. Am. Chem. Soc.* **1995**, *117*, 11780.
(31) Zheng, M.; Dismukes, G. C. *Inorg. Chem.* **1996**, *35*, 3307.
(32) Blondin, G.; Davydov, R.; Philouze, C.; Charlot, M.-F.; Styring, S.; Akermark, B.; Girerd, J.-J.; Boussac, A. *J. Chem. Soc., Dalton Trans.* **1997**, 4069.
(33) Beer, P. D.; Drew, M. G. B.; Leeson, P. B.; Lyssenko, K.; Ogden, M. I. *J. Chem. Soc., Chem. Commun.* **1995**, 929.

over 3 Å molecular sieves. H-2,3-D (= 2,3-dichlorophenoxy-acetic acid), Hpko, dpk (= dipyridylketone), NaN_3, and $MnCl_2 \cdot 4H_2O$ were purchased from Aldrich Co. All chemicals and solvents were reagent grade.

Synthesis of $Mn^{II}_3Mn^{IV}(O)(pko)_4(2,3\text{-}D)_4(CH_3OH)_3$, 1. Into 100 mL of freshly distilled methanol was dissolved 10 mmol of $MnCl_2 \cdot 4H_2O$ (1.980 g), and 10 mmol of Hpko (1.710 g) was added. The reaction mixture was stirred for 20 min. A total of 10 mmol of the sodium salt of 2,3-D (2.44 g) dissolved in a small amount (~20 mL) of methanol was added dropwise followed by the addition of 10 (0.4 g) mmol of NaOH under stirring. The mixture was stirred for 1 h until the solution color became dark red-brown. The resulting dark red-brown solution was reduced to a volume of 40 mL after 5 h of stirring. Black/brown crystals suitable for X-ray diffraction studies were obtained by slow evaporation. Yield: 50%. Analytical data: fw = 2004.78. Anal. calcd for $C_{79}H_{64}Cl_8Mn_4N_{12}O_{20}$: C, 47.28%; H, 3.19%; N, 8.37%; Mn, 10.97%. Found: C, 47.44%; H, 2.90%; N, 9.05%; Mn, 10.60%. IR (KBr pellet, cm^{-1}): $\nu(C{=}N)_{pko}$, 1585(vs); $\nu_{asym}(CO_2)_{2,3\text{-}D}$, 1617(vs); $\nu_{sym}(CO_2)_{2,3\text{-}D}$, 1424(s); $\nu(N{-}O_{ox})_{pko}$, 1267(s). UV/vis λ(nm) (ϵ, $dm^3\ mol^{-1}\ cm^{-1}$): CH_2Cl_2 solution, 622(30).

Synthesis of $Mn^{II}_2Mn^{III}_2(pko)_2(pdiol)(N_3)_6(CH_3OH)_2$, 2. Into 100 mL of freshly distilled methanol was dissolved 10 mmol of $MnCl_2 \cdot 4H_2O$ (1.980 g), and 5 mmol of Hpko (0.855 g) and 2.5 mmol (0.39 g) of dpk were added. A total of 30 mmol (1.95 g) of sodium azide salt dissolved in 10 mL methanol was added. The reaction mixture was stirred for 3 h, and the resulting dark red-brown solution was left at ambient temperature. Red/black crystals suitable for X-ray diffraction studies were obtained by slow evaporation after 2 days. Yield: 60%. Analytical data: fw = 1132.6. Anal. calcd for $C_{35}H_{32}Mn_4N_{26}O_6$: C, 37.08%; H, 2.82%; N, 32.13%; Mn, 19.42%. Found: C, 36.80%; H, 3.00%; N, 33.05%; Mn, 19.05%. IR (KBr pellet, cm^{-1}): $\nu(N{\equiv}N)$, 2077 (vs, triple split); $\nu(C{=}N)_{pko}$, 1594 (vs); $\nu(C{=}N)_{py}$, 1564 (s); $\nu(N{-}O_{ox})_{pko}$, 1469(s).

Physical Measurements. Infrared spectra (200−4000 cm^{-1}) were recorded on a Perkin-Elmer FT-IR 1650 spectrometer with samples prepared as KBr pellets. UV/vis spectra were recorded on a Shimadzu-160A dual-beam spectrophotometer. C, H, and N elemental analyses were performed on a Perkin-Elmer 240B elemental analyzer. Electric conductance measurements were carried out with a WTW model LF 530 conductivity outfit and a type C cell, which had a cell constant of 0.996. This represents a mean value calibrated at 25 °C with potassium chloride. Variable-temperature and variable-field dc magnetic susceptibility measurements were made on powered samples suspended in an eicosane mull. Data were collected on a Quantum Design MPMS SQUID susceptometer. Variable-temperature measurements were collected over a range of 2−300 K at 2500 G. Variable-field measurements were collected over a range of 0−5.5 T at 4.5 K. Variable-temperature ac magnetic susceptibility measurements were collected on powdered samples on a Quantum Design MPMS SQUID susceptometer located in the Physics and Astronomy Department at Michigan State University. Measurements were collected over a range of 2−10 K with a 3.5 G oscillating ac magnetic field and no applied dc magnetic field. The ac magnetic field frequencies were varied from 1 to 1000 Hz. Data were corrected for sample holder contribution and diamagnetism of the sample using Pascal's constants.

XAS Data Collection and Analysis. XAS data for the Mn K-edge were collected at the Stanford Synchrotron Radiation Laboratory on beam line 9-3. The beam energy was 3 GeV, and the beam size was 1 × 4 mm^2. Data were measured in transmission mode, using a Si(220) double-crystal monochromator with a harmonic rejection mirror set to a 10 keV cutoff. Samples were diluted in boron nitride (approximately a 1:1 volume ratio), ground to homogeneity, and packed into 1-mm-thick Al cells with Kapton windows. The sample temperature was maintained at 6.7−7.0 K during data collection using an Oxford liquid helium flow cryostat. Spectra were measured with 10 eV increments in the pre-edge region (6300−6520 eV), 0.35 eV increments in the edge region (6520−6570 eV), and 0.05 $Å^{-1}$ increments (2.75−20 $Å^{-1}$) in the extended X-ray absorption fine structure (EXAFS) region, with integrating times of 1 s in the pre-edge and edge regions and of 1−20 s (k^3, weighted) in the EXAFS region, for a total scan time of 45 min. The X-ray energies were calibrated by simultaneously collecting the absorption spectrum of a $KMnO_4$ sample placed between the second and third ion chambers, with the pre-edge peak assigned as 6453.3 eV. In order to minimize X-ray exposure, a 2 mm Al shutter was used to block the beam during the monochromator move. For all samples, the first and last spectra were compared to confirm the lack of radiation damage during the measurements.

XANES was normalized by fitting a single polynomial below and above the edge with a scale factor to give optimal agreement with tabulated X-ray cross-sections.[34] The edges were fit using a parametrized Voigt profile to model the 1s−3d region and the primitive of a Voigt function to model the rising edge.[35] The complete XANES region was fit as described previously using a library of Mn^{II}, Mn^{III}, and Mn^{IV} model compounds.[8]

The EXAFS was extracted using a three-region cubic spline and fitted to eq 1:

$$\chi(k) = S\sum_i \frac{N_i A_i(k)}{kR_i^2} \exp\left(-2k^2\sigma_i^2\right) \sin[2kR_i + \varphi_i(k)] \qquad (1)$$

where $\chi(k)$ is the fractional modulation in the absorption coefficient above the edge, S is a scale factor, N_i is the number of scatterers at a distance of R_i, $A_i(k)$ is the effective backscattering amplitude, σ_i^2 is the mean-square deviation in R_i, $\varphi_i(k)$ is the phase-shift that the photoelectron wave undergoes in passing through the potentials of the absorbing and scattering atoms, and the sum is taken over all shells of scatters. The amplitude and phase functions were calculated with FEFF 7.02. Fourier transforms were calculated using k^3-weighted data and were not corrected for the EXAFS phase-shift. As a consequence, peaks are shifted by *ca.* 0.4 Å to lower R values relative to the true metal−ligand distance.

Structure Determination for 1. Black needles of **1** were crystallized from a methanol solution at 25 °C. A crystal of dimensions 0.12 × 0.02 × 0.02 mm was mounted on a standard Bruker SMART CCD-based X-ray diffractometer equipped with an LT-2 low-temperature device and normal-focus Mo-target X-ray tube (λ = 0.710 73 A) operated at 2000 W power (50 kV, 40 mA). The X-ray intensities were measured at 150(2) K; the detector was placed at a distance of 4.954 cm from the crystal. A total of 2218 frames were collected with a scan width of 0.3° in ω and φ with an exposure time of 90 s/frame. The frames were integrated with the Bruker SAINT software package with a narrow frame algorithm. The integration of the data yielded a total of 20 264 reflections to a maximum 2θ value of 42.92°, of which 9041 were independent and 3818 were greater than $2\sigma(I)$. The final cell constants (Table 1) were based on the *xyz* centroids of 1021 reflections above $10\sigma(I)$. Analysis of the data showed negligible decay during data collection; the data were processed with SADABS and corrected for absorption.

(34) Weng, T.-C.; Waldo, G. S.; Penner-Hahn, J. E. *J. Synchrotron Radiat.* **2005**, *12*, 506.
(35) Teodorescu, C. M.; Esteva, J. M.; Karnatak, R. C.; Elafif, A. *Nucl. Instrum. Methods* **1994**, *345*, 141.

Table 1. Crystal Data and Structure Refinement for **1** and **2**

	1	2
empirical formula	$C_{79}H_{64}Cl_8Mn_4N_{12}O_{20}$	$C_{70}H_{64}Mn_8N_{52}O_{12}$
fw	2004.78	2265.25
temp	150(2) K	123(2) K
wavelength	0.71073 Å	0.71073 Å
cryst syst	triclinic	monoclinic
space group	$P\bar{1}$	$P2(1)/c$
a	15.664(4) Å	10.7943(6) Å
b	16.770(5) Å	26.6244(17) Å
c	17.162(5) Å	15.7716(9) Å
α	105.233(10)°	90°
β	97.546(11)°	95.4850(10)°
λ	91.500(12)°	90°
volume	4303(2) Å^3	4511.9(5) Å^3
Z	2	2
density (calculated)	1.547 mg/m^3	1.667 mg/m^3
abs coeff	0.899 mm^{-1}	1.171 mm^{-1}
F(000)	2036	2288
cryst size	0.12 × 0.02 × 0.02 mm	0.22 × 0.20 × 0.10 mm
λ range for data collection	2.83−20.99°	2.84−26.44°
limiting indices	$-15 \le h \le 15, -16 \le k \le 16, -17 \le l \le 17$	$-13 \le h \le 13, -33 \le k \le 33, -19 \le l \le 19$
reflns collected/unique	9039/9039 [R(int) = 0.1764]	41546/9244 [R(int) = 0.0765]
completeness to *λ*	20.99 97.9%	26.44 99.5%
refinement method	full-matrix l/s on F^2	full-matrix l/s on F^2
data/restraints/parameters	9039/0/1115	9244/0/768
goodness-of-fit on F^2	0.997	0.967
final R indices [I > 2σ(I)]	R1[a,b] = 0.0885, wR2[a,c] = 0.1880	R1[a,b] = 0.0462, wR2[a,c] = 0.1108
R indices(all data)	R1[a,b] = 0.2200, wR2[a,c] = 0.2488	R1[a,b] = 0.0910, wR2[a,c] = 0.1275
largest diff. peak and hole	0.850 and −0.774 *e* Å^{-3}	0.504 and −0.477 *e* Å^{-3}
max. and min. transmission	0.9822 and 0.8998	0.8919 and 0.7827
abs correction	semiempirical from equivalents	semiempirical from equivalents
extinction coefficient	0.0066(8)	0.00010(10)

[a] 18 317 unique data with $I > 2\sigma(I)$. [b] $R_1 = \sum(|F_o| - |F_c|)/\sum|F_o|$. [c] $wR_2 = [\sum[w(F_o^2 - F_c^2)^2]/\sum[w(F_o)^2]]^{1/2}$; $w = 1/[\sigma^2(F_o^2) + (mp)^2 + np]$; $p = [\max(F_o^2,0) + 2F_c^2]/3$ (*m* and *n* are constants); $\sigma = [\sum[w(F_o^2 - F_c^2)^2]/(n - p)]^{1/2}$.

The structure was solved and refined with the Bruker SHELXTL (version 5.10)[36–38] software package, using the space group $P\bar{1}$ with $Z = 2$ for the formula $C_{79}H_{64}N_{12}O_{20}Cl_8Mn_4$. All non-hydrogen atoms were refined anisotropically with the hydrogen atoms placed in idealized positions. Full-matrix least-squares refinement based on F^2 converged at R1 = 0.0885 and wR2 = 0.1880 [based on $I > 2\sigma(I)$] and at R1 = 0.2200 and wR2 = 0.2488 for all data. Additional details are presented in Table 1 and are given in the Supporting Information as a CIF file.

Structure Determination for 2. Black/red irregular crystals of **2** were crystallized from a methanol solution at 25 °C. A crystal of dimensions 0.22 × 0.20 × 0.10 mm was mounted on a standard Bruker SMART CCD-based X-ray diffractometer equipped with an LT-2 low-temperature device and normal-focus Mo-target X-ray tube (*λ* = 0.710 73 A) operated at 2000 W power (50 kV, 40 mA). The X-ray intensities were measured at 123(2) K; the detector was placed at a distance of 4.954 cm from the crystal. A total of 2193 frames were collected with a scan width of 0.3° in *ω* and *φ* with an exposure time of 30 s/frame. The frames were integrated with the Bruker SAINT software package with a narrow frame algorithm. The integration of the data yielded a total of 41 546 reflections to a maximum 2*θ* value of 53.04°, of which 9465 were independent and 5721 were greater than $2\sigma(I)$. The final cell constants (Table 1) were based on the *xyz* centroids of 4347 reflections above $10\sigma(I)$. Analysis of the data showed negligible decay during data collection; the data were processed with SADABS and corrected for absorption. The structure was solved and refined with the Bruker SHELXTL (version 5.10)[36–38] software package, using the space group $P2(1)/c$ with $Z = 2$ for the formula $C_{70}H_{64}N_{52}O_{12}Mn_8$. All non-hydrogen atoms were refined anisotropically with the hydrogen atoms located on a difference Fourier map and allowed to refine isotropically. The molecule lies on an inversion center in the crystal lattice. Full-matrix least-squares refinement based on F^2 converged at R1 = 0.0462 and wR2 = 0.1108 [based on $I > 2\sigma(I)$] and at R1 = 0.0910 and wR2 = 0.1275 for all data. Additional details are presented in Table 1 and are given in the Supporting Information as a CIF file.

Scheme 1

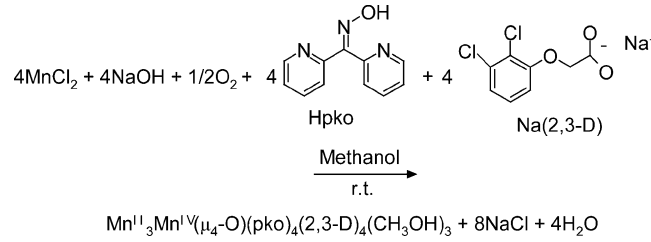

Results

The synthesis of $Mn^{II}_3Mn^{IV}(O)(pko)_4(2,3\text{-}D)_4(CH_3OH)_3$ (**1**) was achieved via the reaction of $MnCl_2 \cdot 4H_2O$ with dipyridylketoxime in a basic solution, followed by the addition of the sodium salt of the phenoxyalkanoic acid in methanol under air, according to the reaction in Scheme 1. The compound is a black-brown crystalline solid, partially soluble in dimethylsulfoxide (DMSO), DMF, CH_2Cl_2, and $CHCl_3$ without electrolytes.

(36) Sheldrick, G. M. *SHELXTL*, v.5.10; Bruker Analytical X-ray: Madison, WI, 1997.
(37) Sheldrick, G. M. *SADABS, Program for Empirical Absorption Correction of Area Detector Data*; University of Gottingen: Gottingen, Germany, 1996.
(38) *Saint Plus*, v.6.02; Bruker Analytical X-ray: Madison, WI, 1999.

Scheme 2

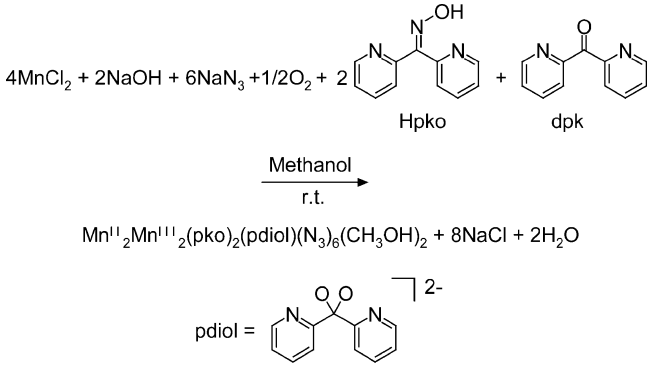

The compound $Mn^{II}_2Mn^{III}_2(pko)_2(pdiol)(N_3)_6(CH_3OH)_2$ (**2**) was synthesized by adding the Hpko ligand and dpk to a solution of $MnCl_2 \cdot 4H_2O$ in methanol. Sodium azide and sodium hydroxide were then dissolved in methanol and added to the manganese/ligand solution (see Scheme 2). $Mn^{II}_2Mn^{III}_2(pko)_2(pdiol)(N_3)_6(CH_3OH)_2$ is a black-brown crystalline solid which is soluble in DMF and DMSO without electrolytes.

Description of the Structure of 1. The central $[Mn_4(\mu_4\text{-}O)]^{8+}$ core of **1** (Figures 1 and 2 and Table 2) is best described as a Mn_4 distorted tetrahedron with one Mn^{IV} ion, Mn1, and three Mn^{II} ions, Mn2, Mn3, and Mn4, in octahedral environments. A μ_4-O atom (O20) bridges the four manganese ions. Four ketoximato N−O moieties bridge the Mn^{IV} ion with the three Mn^{II} ions, while each Mn^{II} ion is bridged with the other two Mn^{II} ion through carboxylato bridges. The Mn···Mn separations fall in the range 3.185−3.625 Å, with the shortest one being between Mn^{II} ions Mn2 and Mn4, which are bridged by a unidentate carboxylato oxygen atom and a bidentate chelate carboxylato ligand, and the longest one being between Mn^{II} ions Mn2 and Mn3, which are bridged only by a bidentate chelate carboxylato ligand. For the Mn^{IV}···Mn^{II} separations, the shortest is 3.294 Å between Mn1 and Mn3, which are bridged by two ketoximato moieties. The dihedral angles around O20 vary from 93.1(4)° up to 120.4(4)°; these are consistent with a distorted tetrahedral geometry and O^{2-} rather than an μ_4-OH group, which prefers the four Mn ions in a square-planar arrangement. All Mn ions show distorted octahedral coordination geometries. Ligation about the Mn^{IV} ion, Mn1, is comprised of four O atoms, three of which are from the ketoximato ligands (O1, O11, and O31) and the fourth from the μ_4-O^{2-} ion (O20), and two N atoms, one from the ketoximato moiety (N22) and the second from a pyridyl nitrogen (N21). Two

Table 2. Selected Metrical Parameters for Complex $Mn^{II}_3Mn^{IV}(O)(pko)_4(2,3\text{-}D)_4(CH_3OH)_3$ **1**

Bond Distances (Å)			
Mn(1)−O(20)	1.782(10)	Mn(3)−O(62)	2.121(11)
Mn(1)−O(11)	1.906(9)	Mn(3)−O(52)	2.166(11)
Mn(1)−O(1)	1.926(10)	Mn(3)−O(21)	2.179(10)
Mn(1)−O(31)	1.928(9)	Mn(3)−O(20)	2.246(9)
Mn(1)−N(21)	2.048(13)	Mn(3)−N(32)	2.278(12)
Mn(1)−N(22)	2.053(13)	Mn(3)−N(31)	2.322(12)
Mn(2)−O(41)	2.109(13)	Mn(4)−O(61)	2.117(10)
Mn(2)−O(51)	2.125(10)	Mn(4)−N(11)	2.262(12)
Mn(2)−O(20)	2.175(9)	Mn(4)−N(12)	2.216(13)
Mn(2)−N(2)	2.258(13)	Mn(4)−O(20)	2.212(9)
Mn(2)−N(1)	2.263(14)	Mn(4)−O(42)	2.140(13)
Mn(2)−O(71)	2.297(10)	Mn(4)−O(71)	2.199(10)
Mn···Mn Separation Distances (Å)			
Mn(1)−Mn(2)	3.38	Mn(2)−Mn(3)	3.62
Mn(1)−Mn(3)	3.29	Mn(2)−Mn(4)	3.19
Mn(1)−Mn(4)	3.47	Mn(3)−Mn(4)	3.56
Angles (deg)			
Mn(1)−O(20)−Mn(2)	116.7(5)	Mn(1)−O(20)−Mn(3)	109.2(4)
Mn(4)−O(20)−Mn(3)	105.9(4)	Mn(2)−O(20)−Mn(4)	93.1(4)
Mn(2)−O(20)−Mn(3)	110.1(4)	Mn(1)−O(20)−Mn(4)	120.4(4)

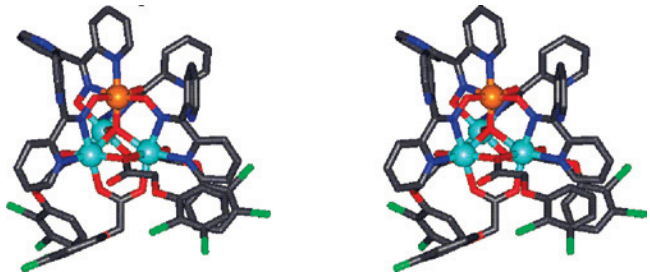

Figure 1. Stereoview of the X-ray crystal structure of **1**. Color scheme: blue sphere, Mn^{II}; orange sphere, Mn^{IV}; red tube, oxygen; blue tube, nitrogen; gray tube, carbon; green tube, chlorine. Hydrogen atoms and the lattice solvent have been removed for clarity.

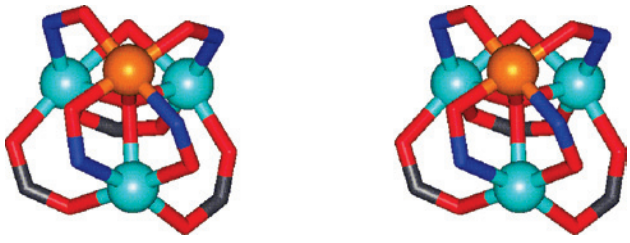

Figure 2. Stereoview of the core of **1**. A μ_4-O^{2-} links together all four manganese ions. In addition, the Mn^{IV} is bridged to all three Mn^{II} ions via O−N linkages. The Mn^{II} ions are connected to each other by O−C−O bridges, and Mn2 is bridged to Mn4 via a μ_2-O. See Figure 1 for the color scheme.

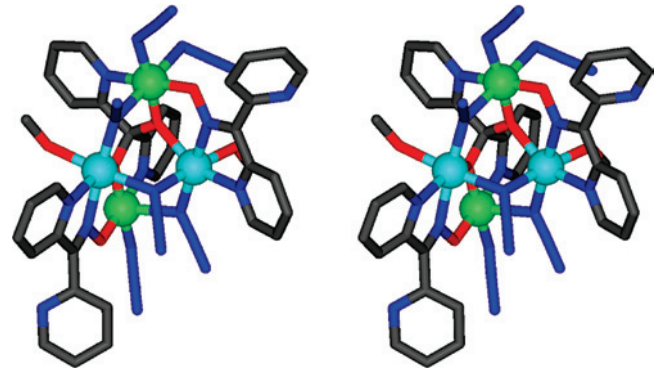

Figure 3. Stereoview of the X-ray crystal structure of **2**. Color scheme: blue sphere, Mn^{II}; green sphere, Mn^{III}; red tube, oxygen; blue tube, nitrogen; gray tube, carbon. Hydrogen atoms and the lattice solvent have been removed for clarity.

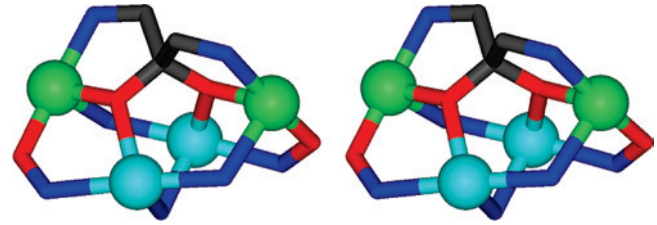

Figure 4. Stereoview of the core of **2**. The Mn^{II} ions are connected to the Mn^{III} ions via N−O linkages. See Figure 3 for the color scheme.

Table 3. Selected Metrical Parameters for Complex $Mn^{II}_2Mn^{III}_2(pko)_2(pdiol)(N_3)_6(CH_3OH)_2$ **2**

Bond Distances (Å)			
Mn(1)−N(18)	2.166(3)	Mn(3)−O(6)	2.181(2)
Mn(1)−N(20)	2.290(3)	Mn(3)−N(23)	2.261(3)
Mn(1)−N(19)	2.272(3)	Mn(3)−N(22)	2.249(3)
Mn(1)−N(12)	2.205(3)	Mn(3)−N(12)	2.243(3)
Mn(1)−O(5)	2.195(2)	Mn(3)−O(1)	2.235(3)
Mn(1)−O(2)	2.182(3)	Mn(3)−N(15)	2.217(4)
Mn(2)−O(4)	1.899(2)	Mn(4)−O(3)	1.886(2)
Mn(2)−N(9)	2.304(3)	Mn(4)−N(15)	2.312(3)
Mn(2)−N(18)	2.273(3)	Mn(4)−N(25)	2.031(3)
Mn(2)−N(26)	2.046(3)	Mn(4)−N(3)	1.940(3)
Mn(2)−N(6)	1.952(3)	Mn(4)−O(5)	1.927(2)
Mn(2)−O(6)	1.934(2)	Mn(4)-N(7a)	2.379(3)
Bond Distances of E−E N_3^- (Å)		Bond Distances of E−O N_3^- (Å)	
N(7)−N(8)	1.194(4)	$N-N_{bound,average}$	1.150
N(8)−N(9)	1.190(4)	$N-N_{unbound,average}$	1.169
Bond Distances of Terminal N_3^- (Å)			
N(1)−N(2)	1.152(5)	N(4)−N(5)	1.137(4)
N(2)−N(3)	1.191(4)	N(5)−N(6)	1.218(4)
Mn···Mn Separation Distances (Å)			
Mn(1)−Mn(2)	3.77	Mn(2)−Mn(3)	3.56
Mn(1)−Mn(3)	3.60	Mn(2)−Mn(4)	5.50
Mn(1)−Mn(4)	3.59	Mn(3)−Mn(4)	3.79
Angles (deg)			
Mn(4)−O(5)−Mn(1)	121.19(11)	Mn(1)−N(12)−Mn(3)	108.18(13)
Mn(2)−O(6)−Mn(3)	119.73(11)	Mn(3)−N(15)−Mn(4)	113.45(16)
Mn(1)−N(18)−Mn(2)	116.24(14)		

of the Mn^{II} ions, Mn2 and Mn4, have $Mn(N_{ketoximato})(N_{pyridyl})(O_{chelatecarboxylato})_2(O_{unidentatecarboxylato})(\mu_4\text{-}O)$ coordination spheres (Mn2: N2, N1, O41 and O51, O71, and O20; Mn4: N12, N11, O42 and O61, O71, and O20), whereas for the third Mn^{II} ion, Mn3, the unidentate carboxylato oxygen is replaced by a ketoximato oxygen (N32, N31, O52 and O62, O21, and O20). The oxidation states of three of the manganese ions, Mn2, Mn3, and Mn4, can be easily assigned as Mn^{II} on the basis of the average Mn−N/O distance of 2.20 Å for Mn2, 2.23 Å for Mn3, and 2.08 Å for Mn4. The distances around Mn1 range from 1.782(10) to 2.053(13) Å, with an average Mn−N/O distance of 1.94 Å, consistent with Mn^{IV}. Further evidence that Mn1 is Mn^{IV} rather than Mn^{III} comes from a closer examination of the coordination environment. This shows a distorted octahedral geometry with a very short distance, Mn1−O = 1.782(10) Å, and the longest along the same axis on the opposite apex, Mn1−N21 = 2.053(13) Å. The sum of the axial bonds O−Mn1−N21 = 3.83 Å, O1−Mn1−N22 = 3.979 Å, and O11−Mn1−O31 = 3.834 Å does not suggest an elongation or depression along any axis, in contrast with the expectation for Mn^{III}. The short Mn−O distance of 1.782(10) Å could suggest a Mn=O^- moiety. However, this is inconsistent with the IR data, which do not show a strong band around 1000 cm^{-1}.

Description of the Structure of 2. The overall arrangement of the Mn ions of **2** is best described as a distorted tetrahedron (Figures 3 and 4 and Table 3) with each Mn ion being six-coordinate. Mn1 and Mn3 are in similar ligand environments. The ions are surrounded by one methoxide oxygen (Mn1, O2; Mn3, O1), one pyridyl nitrogen from a pko^- ligand (Mn1, N19; Mn3, N22), two nitrogens from end-on (EO) bridging μ-azide anions (Mn1, N12 and N18; Mn3, N12 and N15), and one oxygen from a $pdol^{2-}$ ligand (Mn1, O5; Mn3, O6). The average M−N/O distances for Mn1 and Mn3 are 2.22 and 2.23 Å, respectively. These distances and a lack of a Jahn−Teller distortion support a 2+ oxidation state for both Mn1 and Mn3. Mn2 and Mn4 are also in similar ligand environments. Three of the nitrogen atoms come from azide anions, though each azide anion has a different coordination mode. One azide binds terminal (Mn2, N6; Mn4, N3), the second is an end-on bridging μ-azide (Mn2, N18; Mn4, N15), and the third is an end-to-end (EE) azide (Mn2, N9; Mn4, N7). The coordination sphere is completed by a pyridyl nitrogen atom (Mn2, N26; Mn4, N25) and an oxygen atom (Mn2, O6; Mn4, O5) from the same $pdol^{2-}$ ligand and an oxygen atom from a different pko^- ligand (Mn2, O4; Mn4, O3). The average M−N/O distances for Mn2 and Mn4 are 2.07 and 2.08 Å, respectively, with a pronounced axial elongation along the $N_{EO}-Mn-N_{EE}$ axis (average Mn−N bond distances are 2.29 Å for Mn2 and 2.34 Å for Mn4). These data support a 3+ oxidation state for both Mn2 and Mn4. The Mn ions are bridged to each other through a series of one- and two-atom bridges. Mn1 is bridged to Mn2 via N18, to Mn3 via N12, and to Mn4 via O5 and the two-atom bridge N20−O3. Mn2 is additionally bridged to Mn3 via O6 and the two-atom bridge O4−N23 and to the Mn4 ion of an adjacent complex via an EE azide. Mn3 is bridged to Mn4 via N15 in addition to the bridges to Mn1 and Mn2. Mn4 is also bridged to the Mn2 of an adjacent complex via an EE azide. The Mn−Mn distances in the complex are Mn1−Mn2, 3.77 Å; Mn1−Mn3, 3.60 Å; Mn1−Mn4, 3.59 Å; Mn2−Mn3, 3.56 Å; Mn2−Mn4, 5.50 Å; and Mn3−Mn4, 3.79 Å.

The two azide anions that bind end-to-end provide bridges to adjacent Mn_4 complexes. This creates a one-dimensional chain in the solid state (Figure 5). Mn4 is bound to a Mn2 ion of the adjacent complex though an EE azide anion (Mn4−N7−N8−N9−Mn2a) with the Mn4−Mn2a distance equal to 6.02 Å.

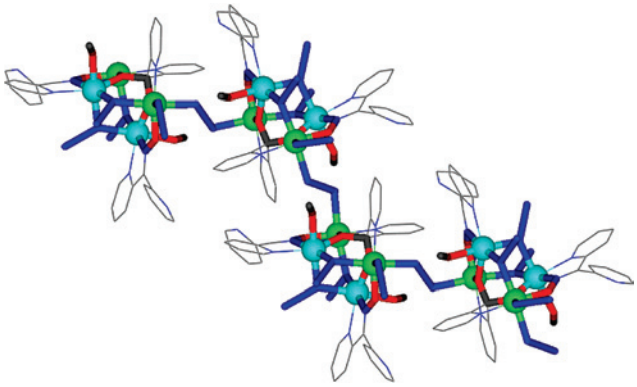

Figure 5. Chain structure of **2**. Adjacent complexes are linked via an azide anion binding end-to-end between Mn^{III} ions. See Figure 3 for the color scheme. Hydrogen atoms and the lattice solvent have been removed for clarity.

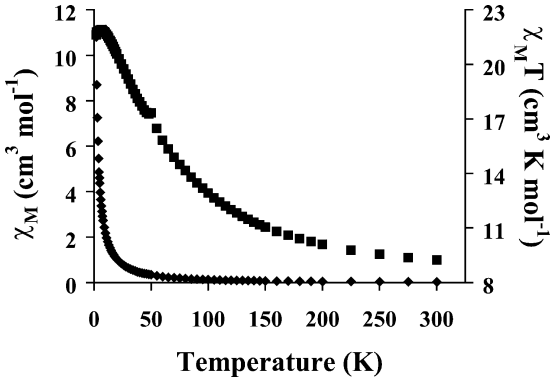

Figure 6. Variable-temperature dc magnetic susceptibility measurements of **1** (◆, χ_M; ■, $\chi_M T$).

Magnetic Properties of 1. Variable-temperature dc magnetic susceptibility measurements indicated that **1** is dominated by ferromagnetic interactions (Figure 6). This is evident by an increase it the χT values from 9.25 cm^3 K mol^{-1} at 300 K to 21.9 cm^3 K mol^{-1} at 6.5 K. Below 6.5 K, χT begins to decrease and falls to 21.6 cm^3 K mol^{-1} at 2 K. This is probably due to a combination of Zeeman and zero-field splitting effects. Variable-field magnetic susceptibility measurements were conducted up to 55 000 G at 4.5 K in an effort to isolate a ground state for **1** (Figure 7). To find the ground spin state, the data were fit to the Brillouin function defined below:

$$M = Ng\beta S\left[\frac{2S+1}{2S}\coth\left(\frac{2S+1}{2S}\times\frac{g\beta SH}{kT}\right) - \frac{1}{2S}\coth\left(\frac{1}{2S}\times\frac{g\beta SH}{kT}\right)\right] \quad (2)$$

where M is the magnetization, N is Avogadro's number, β is the Bohr magneton, k is the Boltzmann constant, S is the ground spin state, H is the applied magnetic field, T is temperature, and the g factor is fixed at 2.0. Fitting the data to the Brillouin function gives a ground spin state of $S = 6$.

Magnetic Properties of 2. Variable-temperature dc magnetic susceptibility measurements of **2** indicate an overall antiferromagnetic interaction (Figure 8). The χT value steadily decreases from 14.1 cm^3 K mol^{-1} at 300 K to 2.90 cm^3 K mol^{-1} at 4.5 K. Variable-field magnetic susceptibility measurements at 4.5 K reveal that no ground state is isolated

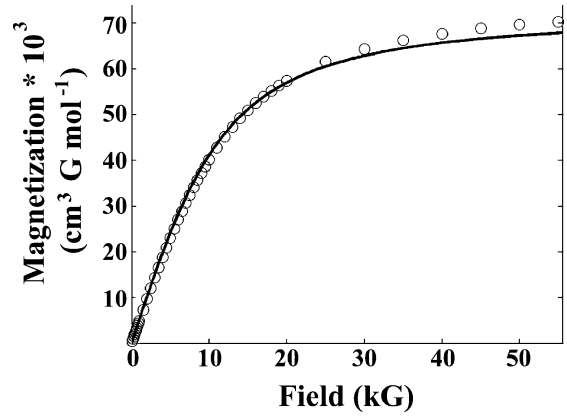

Figure 7. Variable-field dc magnetic susceptibility measurements of **1** at 4.5 K. Fit of the Brillouin function to the magnetization data yields an $S = 6$ ground spin state ($g = 2$).

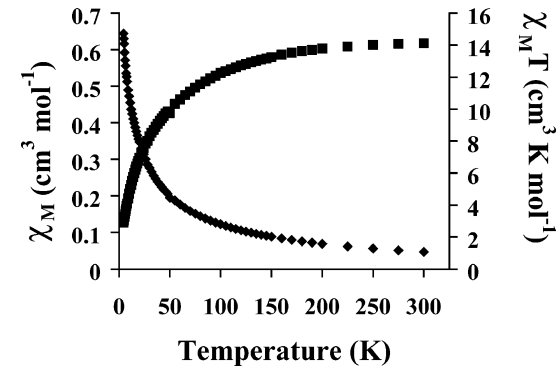

Figure 8. Variable-temperature dc magnetic susceptibility measurements of **2** (◆, χ_M; ■, $\chi_M T$).

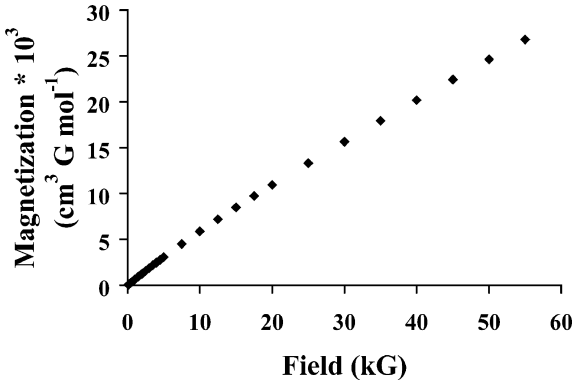

Figure 9. Variable-field dc magnetic susceptibility measurements of **2** at 4.5 K.

(Figure 9). The magnetization increases linearly with increasing applied field (60.39 cm^3 G mol^{-1} at 100 G; 26.79 × 10^3 cm^3 G mol^{-1} at 55 000 G). Since the magnetization of **2** does not saturate under the experimental conditions, no ground state can be determined from these measurements.

Since **2** has a manganese ion arrangement and combination of oxidation states similar to that of other SMMs, we pursued variable-temperature ac magnetic susceptibility measurements to see if **2** behaved as a SMM. At all tested oscillating magnetic fields (1−1000 Hz), the in-phase susceptibility begins to deviate from linearity near 3 K (Figure 10). With this deviation, an out-of-phase susceptibility signal begins to increase near the same temperature (Figure 11). The ac magnetic susceptibility signal is frequency-dependent, sug-

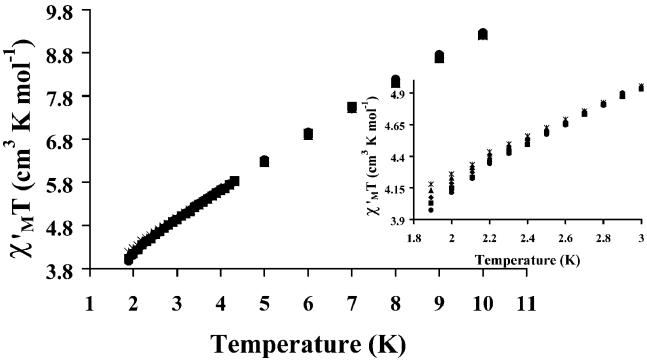

Figure 10. Variable-temperature in-phase ac magnetic susceptibility measurements of **2**. Inset: Low-temperature region displaying the frequency dependence of the in-phase magnetic susceptibility (●, 1000 Hz; ■, 500 Hz; ◆, 100 Hz; ▲, 10 Hz; *, 1 Hz).

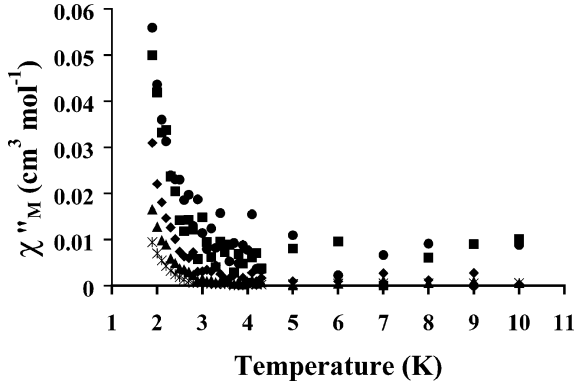

Figure 11. Variable-temperature out-of-phase ac magnetic susceptibility measurements of **2** (●, 1000 Hz; ■, 500 Hz; ◆, 100 Hz; ▲, 10 Hz; *, 1 Hz).

gesting that **2** behaves as a SMM. However, due to the 2 K limit of the instrument, only the tail of the peak is observed, and the blocking temperature cannot be determined from these data. Other $Mn^{II}_2Mn^{III}_2$ complexes have shown similar behavior.[39] In addition, another one-dimensional $Mn^{II}_2Mn^{III}_2$ chain complex has been reported to have a frequency-dependent out-of-phase ac magnetic susceptibility signal below 3 K.[45]

The in-phase magnetic susceptibility increases linearly with an increase in temperature above 4.0 K, suggesting that low-lying excited states are populated.[40] Extrapolating the frequency-independent in-phase magnetic susceptibility data measured above 4.5 to 0 K yields a value of 3.4 cm^3 K mol^{-1} and a predicted ground spin state of $S = 2$ (theoretical $\chi'T$ = 3.0 cm^3 K mol^{-1}).

XANES. Figure 12 shows the normalized XANES spectra for **1**, $Mn^{II}_3Mn^{IV}$, and **2**, $Mn^{II}_2Mn^{III}_2$. Although these compounds have identical formal oxidation states (2.5), they clearly have different XANES spectra, with **1** having a principal absorption peak that is shifted noticeably to lower energy compared to that for **2**. This reflects the fact that Mn^{II}

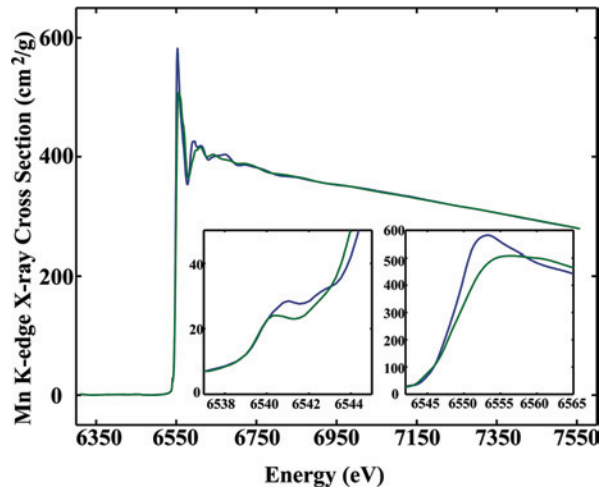

Figure 12. Normalized absorption spectra for **1** (blue, $Mn^{II}_3Mn^{IV}$) and **2** (green, $Mn^{II}_2Mn^{III}_3$), with insets showing the 1s−3d pre-edge region and the XANES region.

compounds tend to have intense maxima, while the XANES spectra for Mn^{III} and Mn^{IV} compounds are both shifted to higher energy and characterized by much broader edge features. There are a variety of ways in which one can estimate edge energy, including fits to the complete edge region,[8,41] calculation of the first inflection point,[42] and an integral method[43] that is related to the first-moment method of Alp et al.[44] As in our earlier studies of mixed-valence trinuclear complexes,[8] the edge-fitting protocol gives the correct average oxidation state of 2.5 within the estimated uncertainty of ∼±0.25 (2.31−2.38 for **1**, 2.65−2.8 for **2**), although the differences between these valence isomers is larger than seen previously (2.47−2.76 for $Mn_2^{II}Mn^{IV}$ (**3**)[8] vs 2.59−2.87 for $Mn^{II}Mn_2^{III}$ (**4**),[8] see Table S1, Supporting Information). For both the trinuclear and the tetranuclear pairs of valence isomers, the edge fits for the complexes containing $Mn^{II}Mn^{IV}$ have an apparent average oxidation state that is slightly (0.1−0.3) lower than that for the complexes containing Mn_2^{III}. As in the previous work on the trinuclear complexes, fits using the correct set of oxidation state models (Mn^{II}+Mn^{IV} for **1**, Mn^{II}+Mn^{III} for **2**) give the best fits and a more accurate estimate of the oxidation state.

The differences in apparent oxidation state of valence isomers are larger if the oxidation state is estimated using either Dau et al.'s integral method[43] with $\mu_1 = 0.15$ and $\mu_2 = 1.0$ (0.78 eV for **1** vs **2**, 0.7 eV for **3**-SCN vs **4**, 1.0 eV for **3**-Cl vs **4**) or the inflection point (0.60 eV for **1** vs **2**, 0.5 eV for **3**-SCN vs **4**, 2.8 eV for **3**-Cl vs **4**). The larger variability using first inflection points reflects the pronounced

(39) (a) Bhattacharjee, A.; Miyazaki, Y.; Nakano, M.; Yoo, J.; Christou, G.; Hendrickson, D. N.; Sorai, M. *Polyhedron* **2001**, *20*, 1607. (b) Yoo, J.; Yamaguchi, A.; Nakano, M.; Krzystek, J.; Streib, W. E.; Brunel, L.-C.; Ishimoto, H.; Christou, G.; Hendrickson, D. N. *Inorg. Chem.* **2001**, *40*, 4604. (c) Wittick, L. M.; Murray, K. S.; Moubaraki, B.; Batten, S. R.; Spiccia, L.; Berry, K. J. *Dalton Trans.* **2004**, 1003.
(40) Chakov, N. E.; Wernsdorfer, W.; Abboud, K. A.; Christou, G. *Inorg. Chem.* **2004**, *43*, 5919.
(41) Riggs, P. J.; Mei, R.; Yocum, C. F.; Penner-Hahn, J. E. *J. Am. Chem. Soc.* **1992**, *114*, 10650.
(42) Messinger, J.; Robblee, J. H.; Bergmann, U.; Fernandez, C.; Glatzel, P.; Visser, H.; Cinco, R. M.; McFarlane, K. L.; Bellacchio, E.; Pizarro, S. A.; Cramer, S. P.; Sauer, K.; Klein, M. P.; Yachandra, V. K. *J. Am. Chem. Soc.* **2001**, *123*, 7804.
(43) Haumann, M.; Muller, C.; Liebisch, P.; Iuzzolino, L.; Dittmer, J.; Grabolle, M.; Neisius, T.; Meyer-Klaucke, W.; Dau, H. *Biochemistry* **2005**, *44*, 1894.
(44) Alp, E. E.; Goodman, G. L.; Soderholm, L.; Mini, S. M.; Ramanathan, M.; Shenoy, G. K.; Bommannavar, A. S. *J. Phys.: Condens. Matter* **1989**, *1*, 6463.
(45) King, P.; Wernsdorfer, W.; Abboud, K. A.; Christou, G. *Inorg. Chem.* **2004**, *43*, 7315.

sensitivity of the first inflection point to the shape of the XANES spectrum. Although the absolute difference is larger, if one converts these differences to changes in apparent oxidation state, the results are very similar to that found for the edge fits. Thus, if the typical change in edge energy is taken as ~3 eV/electron (i.e., ~0.75 eV shift for each oxidation of a tetranuclear complex and ~1.0 eV shift for each oxidation of a trinuclear complex), the apparent change in oxidation state for $Mn^{II}Mn^{IV}$ versus Mn_2^{III} valence isomers corresponds to oxidation of ~1 Mn, that is, to a change in apparent average oxidation state of ~0.3.

EXAFS. As is apparent from Tables 2 and 3, both **1** and **2** have complex distributions of nearest neighbors and extremely complex distributions of outer-shell scatterers. In order to simplify the analysis, we have focused solely on the nearest-neighbor scatterers. Attempts to fit the data using a single shell were not successful, giving poor fits and anomalously low apparent coordination numbers. Although the EXAFS data were measured to moderate resolution (k_{max} = 15 Å^{-1}; $\Delta R \sim 0.1$ Å), the number of independent degrees of freedom for the first shell ($N_{idp} = 2\,\Delta k \Delta R/\pi \approx 10$) is too small to permit refinement of more than two shells of scatterers. Attempts to fit the data using two shells of scatterers gave reasonable fits (see Figure S1, Supporting Information), using the parameters given in Table S2 (Supporting Information). For these fits, the total coordination number was constrained to be 6. In both cases, one shell of Mn−O refines to ~1.9 Å, in reasonable agreement with fact that both compounds contain several short Mn−O distances. However, none of these fits are particularly satisfying, probably reflecting the inherent difficulty of fitting the EXAFS data for mixed valence complexes—the average Mn−ligand distance is reasonably well defined and is in good agreement with the expected value, but the details of the ligation geometry are nearly impossible to determine experimentally. The origin of this difficulty is illustrated by Figure S2 (Supporting Information), which shows a histogram of the nearest neighbor distances for **1** and **2**. Although these can be divided, somewhat arbitrarily, into two shells of 1:5 or 2:4 scatterers, respectively, it is obvious that neither distribution is well-defined by two shells of scatterers. As an alternative, we explored our ability to simulate the EXAFS using the known crystallographic coordinates. In order to obtain the best fit while minimizing the number of variable parameters, we refined a single Debye−Waller factor for all nearest neighbors. This gives a good fit to the data (Figure S3, Supporting Information), comparable to the two-shell fits but with only a single variable parameter. This confirms the integrity of both **1** and **2**, and the validity of our interpretation of the EXAFS, and highlights the difficulty of fitting EXAFS spectra for low-symmetry, mixed-valence complexes.

Discussion

Magnetic Properties. The magnetic behavior of **1** is very similar to that of a previously reported complex, $[Mn^{II}_3Mn^{IV}(O)(pko)_4(3,4\text{-}D)_4]\cdot 2.5CH_3OH$ (**5**), which was synthesized by one of us.[25] Both complexes have an $S = 6$ ground spin state and are dominated by ferromagnetic exchange among the manganese ions; however, the J coupling parameters for **1** could not be determined as for **5**. Though, since **1** has similar variable-temperature dc magnetic susceptibility values and the same ground spin state as **5**, one can presume that the coupling is very comparable. The manganese oxidation states and connectivity are exactly the same; the only difference is the ligand used to construct the complex. In **1**, the ligand contains chlorine atoms located at positions 2 and 3 on the dichlorophenoxy acetate ligand, while in **5** the chlorine atoms are at the 3 and 4 positions. Repeated attempts to fit the variable-temperature magnetic susceptibility data of **1** failed; however, it can be estimated on the basis of structural similarity, similar ground spin states, and the similar behavior of the variable-temperature dc magnetic susceptibility measurements that the magnetic coupling scheme of **1** is the same as that of **5**, but the magnitudes of the J values are different. In **5**, the Mn^{IV} ion is strongly ferromagnetically coupled to the two closest Mn^{II} ions and weakly ferromagnetically coupled to farthest Mn^{II} ion, while two of the Mn^{II} ions, which are at the shortest Mn−Mn distance in the complex, are weakly antiferromagnetically coupled to each other.

The dc magnetic susceptibility measurements of **2** indicate that the structure is dominated by antiferromagnetic interactions among the manganese ions. A ground spin state could not be determined from dc measurements, but ac magnetic susceptibility measurements estimate a ground spin state of $S = 2$. The frequency-dependent ac magnetic susceptibility measurements indicate that **2** may behave as a SMM. The ground spin state of **2** is small, but other SMMs have been reported with such ground spin states.[45] The observed frequency-dependent ac magnetic susceptibility signal, however, may be due to magnetic ordering or glassy magnetic behavior; without lower-temperature data and observed magnetic hysteresis, it is difficult to eliminate these other possibilities. However, this possible SMM behavior in **2**, together with the existence of other manganese tetramers that behave as SMMs,[46] raises the interesting question of whether the OEC in certain S states might also behave as an SMM.

Near-Edge Shape. The shapes, and thus the apparent edge energies, for **1** and **2** are significantly different. Although both complexes have the same average formal oxidation state, this increase in Mn^{II} absorption results in a shift in the edge energy of ~0.6−0.8 eV. In principle, this might be caused by radiation damage, if this were significantly more severe for compound **1**. However, we did not see any change between the first scan and second scan, meaning that, if radiation damage took place, it would have to be complete during the pre-edge region of the first scan (<1 min of X-ray exposure). We know of no example in which cryogenic solids are photoreduced this rapidly. Moreover, variable-field dc magnetic susceptibility measurements of **1** + boron nitride show a magnetization pattern and values similar to those of a nonirradiated sample. Consequently, we conclude that this

(46) (a) Christou, G.; Gatteschi, D.; Hendrickson, D. N.; Sessoli, R. *MRS Bull.* **2000**, *25*, 66. (b) Gatteschi, D.; Sessoli, R. *Angew. Chem., Int. Ed.* **2003**, *42*, 268.

shift in edge energy represents an authentic property of **1**.

Depending on the structures and ligand types, XAS spectra for Mn^{II} compounds usually have a principle absorption peak centered between 6551 and 6554 eV with an intensity varying from 550 to 700 cm^2/g.[47] For higher-valent manganese ions, the principle absorption peaks center at higher energies with intensities varying from 450 to 550 cm^2/g. Since **1** contains more Mn^{II} than **2**, the absorption at ~6552 eV for **1** is expected to be higher, which is consistent with the experimental results.

We[41] and others[42,43,48] have previously suggested that Mn edge energy should be a good measure of average Mn oxidation state. While this has been amply validated for studies of Mn^{III} and Mn^{IV} complexes, the present results, together with our earlier studies,[8] demonstrate that this is not necessarily true if there is significant Mn^{II} present in a sample. In these cases, we find that conversion of Mn_2^{III} to $Mn^{II}Mn^{IV}$ and reduction by one electron have similar effects on the edge energy.

This has important implications for understanding the oxidation states in the photosynthetic oxygen-evolving complex. Although there is now general consensus that the S_1 state is $Mn_2^{III}Mn_2^{IV}$, there remains ambiguity regarding the S_0 state. Early EPR measurements of S_0 were interpreted as suggesting that Mn^{II} was present,[49] although more recent ^{55}Mn electron nuclear double-resonance measurements suggest that S_0 is $Mn_3^{III}Mn^{IV}$;[50,51] XANES measurements for S_0 have been interpreted as consistent with, but not proof of, the presence of Mn^{II}. These differences reflect uncertainty in the oxidation state of two of the Mn ions in the OEC, since either $Mn^{II}Mn^{IV}$ or $Mn^{III}Mn^{III}$ would be consistent with the observed XANES, EXAFS, and EPR. Our data allow us to explore this difference for tetranuclear models, although our models represent the S_{-3} state of the OEC rather than the S_0 state.

Although the published XANES spectra for S_0[42,43] are nearly identical, the estimated energy difference for S_0-S_1 depends strongly on whether one uses an integral method (0.58 eV[43]) or the first inflection point (2.1 eV[42]) to estimate the edge energy. In both cases, the difference between S_0 and S_1 is very similar to the differences that we see between mixed-valence isomers. Thus, the observed S_0-S_1 difference could arise from valence isomerization with no net change in oxidation state. However, this is inconsistent with EPR data showing that S_0 has a half-integer spin while S_1 has an integer spin. Given that S_0 must be reduced relative to S_1, our data favor the presence of $Mn_3^{III}Mn^{IV}$ in S_0; if it were $Mn^{II}Mn^{III}Mn_2^{IV}$, the combined effect of reduction and formation of Mn^{II} should give an even larger edge shift than is observed.

Conclusion

We have prepared tetranuclear Mn valence isomers that have allowed us to explore the effect of valence isomerization on the XANES. These results, which are similar to earlier results for trinuclear valence isomers, show that, at least in these cases, XANES spectra cannot readily discriminate between $Mn^{II}Mn^{IV}$ and $Mn^{III}Mn^{III}$ units in multinuclear complexes, with estimates based on the first inflection point energy being particularly problematic. For trinuclear complexes, the change in average oxidation state per Mn oxidation step (0.33) was large enough that we were able to distinguish between models for the overall oxidation state on the basis of XANES fits. For tetranuclear complexes, the change in oxidation is sufficiently small (0.025) so that this distribution is not reliably identifiable on the basis of XANES alone, although XANES combined with EPR remains definitive. On the basis of published data for the S_0-S_1 conversion, our spectra suggest that this does not involve both a valence isomerization (e.g., $Mn^{III}_2 \rightarrow Mn^{II}Mn^{IV}$) and an oxidation, thus favoring a $Mn_3^{III}Mn^{IV}$ oxidation state in S_0.

Acknowledgment. The authors wish to thank the following agencies for support of this research: VLP (NIH GM39406), DK (WG010 of D21 COST action and PENED 2001), and JEPH (NIH GM45205). We thank Reza Loloee and the Physics and Astronomy Department at Michigan State University for the use of their Quantum Design MPMS SQUID magnetometer.

Supporting Information Available: CIF files for **1** and **2** and detailed fits to the EXAFS and XANES of **1** and **2**. This material is available free of charge via the Internet at http://pubs.acs.org.

IC702109C

(47) Stemmler, T. L.; Sossong, T. M.; Goldstein, J. I.; Ash, D. E.; Elgren, T. E.; Krutz, D. M.; Penner-Hahn, J. E. *Biochemistry* **1997**, *36*, 9847.
(48) Kirby, J. A.; Goodin, D. B.; Wydrzynski, T.; Robertson, A. S.; Klein, M. P. *J. Am. Chem. Soc.* **1981**, *103*, 5537.
(49) Messinger, J.; Nugent, J. H. A.; Evans, M. C. W. *Biochemistry* **1997**, *36*, 11055.
(50) Kulik, L. V.; Epel, B.; Lubitz, W.; Messinger, J. *J. Am. Chem. Soc.* **2005**, *127*, 2392.
(51) Kulik, L. V.; Epel, B.; Lubitz, W.; Messinger, J. *J. Am. Chem. Soc.* **2007**, *129*, 13421.